

Supporting Information

Nitrogen containing carbon spheres as an efficient electrocatalyst for oxygen reduction: Microelectrochemical investigation and visualization

*Aarti Tiwari, Vikram Singh, Debaprasad Mandal and Tharamani C. Nagaiah**

Department of Chemistry, Indian Institute of Technology Ropar, Rupnagar, Punjab-140001, India.

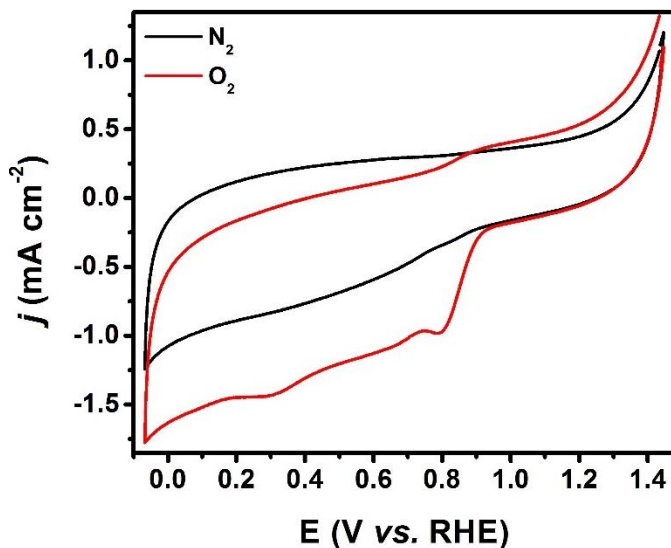


Fig. S1. Cyclic voltammogram of NCS-800 in N₂ and O₂ purged 1 M NaOH electrolyte respectively at a scan rate of 25 mV/s. CE: Pt-mesh; RE: Hg/HgO/1 M NaOH. (potentials converted to RHE scale)

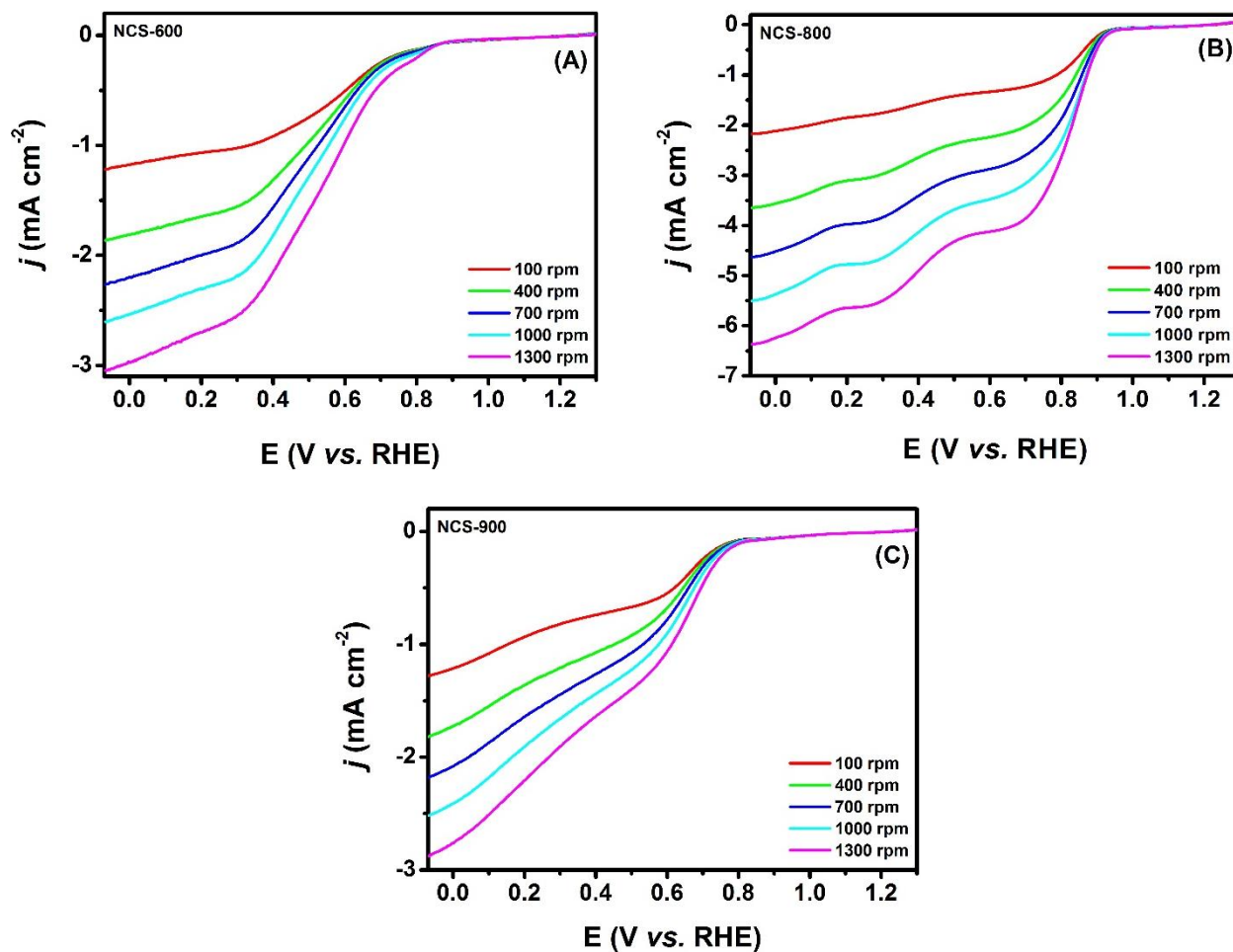


Fig. S2. RDE Linear polarization curves for (a) NCS-600, (b) NCS-800 and (c) NCS-900 at varying rotation rates in 1 M NaOH at a scan rate of 5 mV/s. CE: Pt-mesh; RE: Hg/HgO/1 M NaOH. (potentials converted to RHE scale)

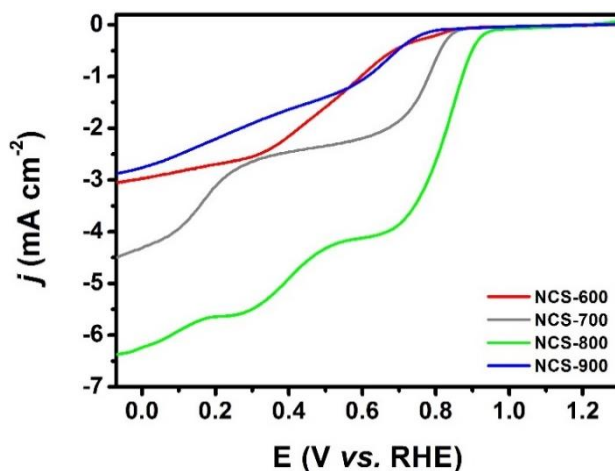


Fig. S3. RDE Linear polarization curves for NCS-600, NCS-700, NCS-800 and NCS-900 at 1300 rpm in oxygen saturated 1 M NaOH at a scan rate of 5 mV/s. CE: Pt-mesh; RE: Hg/HgO/1 M NaOH. (potentials converted to RHE scale)

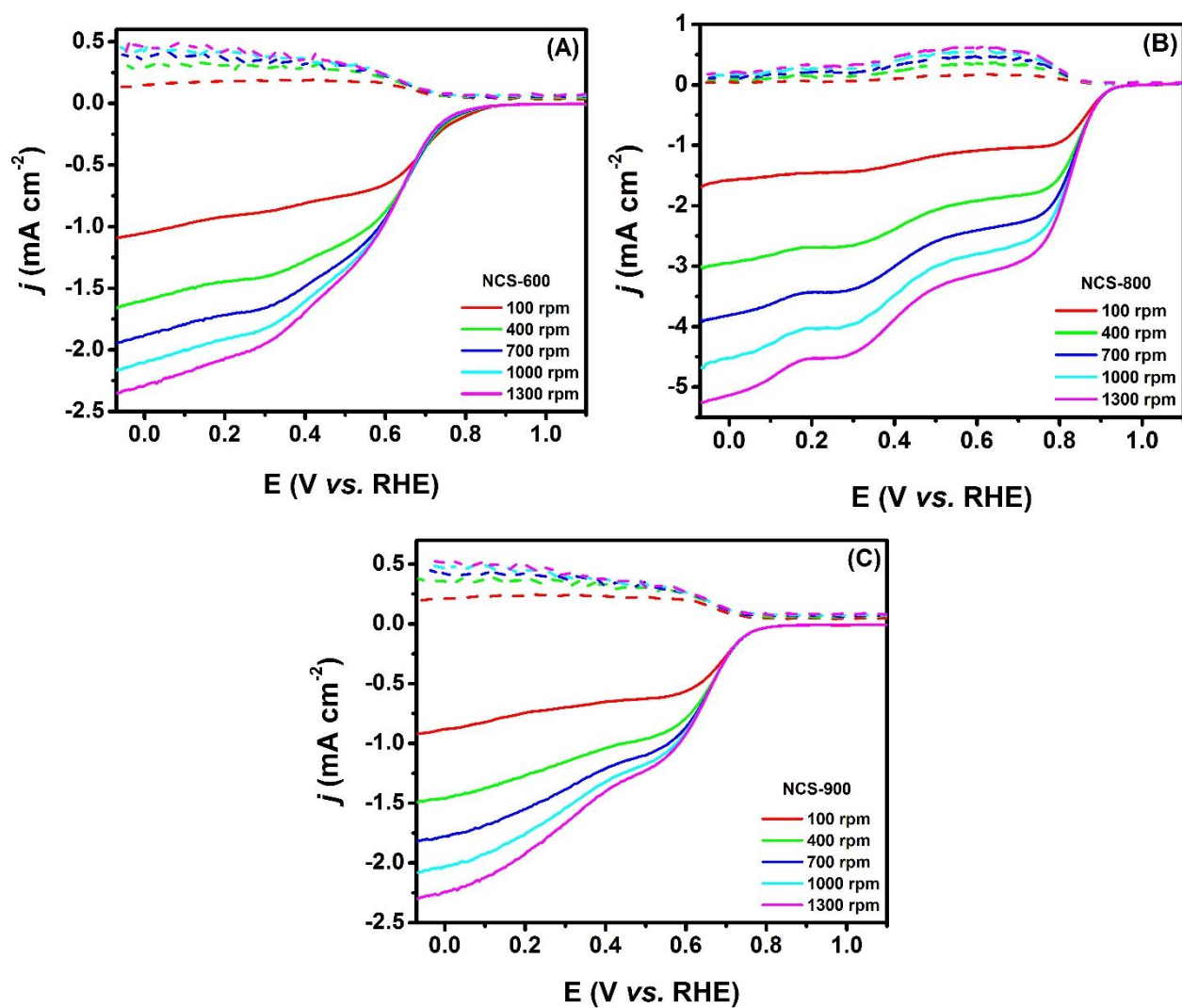
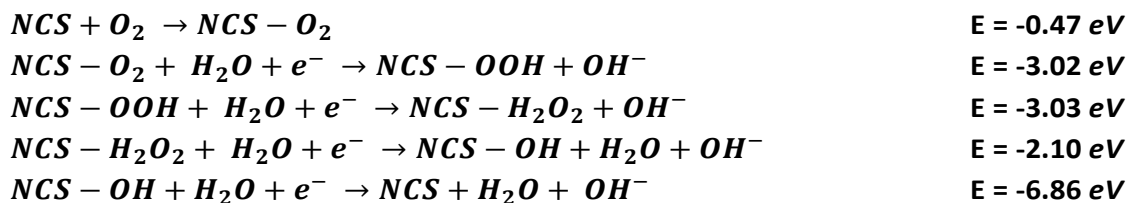


Fig. S4. Rotating ring-disk voltammograms for oxygen reduction in oxygen saturated 1 M NaOH for (a) NCS-600, (b) NCS-800 and (c) NCS-900 catalysts at a scan rate of 5 mV/s and varying rotation rates. CE: Pt-mesh; RE: Hg/HgO/1 M NaOH. (potentials converted to RHE scale)

➤ Density functional theory calculation

Gaussian 09 program¹ was used to perform density functional theory (DFT) calculations and the geometries of NCS catalyst were fully optimized by using the Lee-Yang-Parr correlation functional (B3LYP)² by considering the solvation effects of water in IEFPCM model. Standard 6-31G+ (d,p) basis set was used for all the atoms.

The NCS catalyst and the related nitrogen-free variant was fully optimized and its subsequent interaction with oxygen was studied. The detailed reaction steps and the resulting reaction energies are as follows (also depicted in Fig. 3, manuscript):



The reaction energies indicate that ORR over the NCS catalyst is a downhill process involving the formation of H₂O₂ species and its further reduction to water which is thermodynamically facile as observed experimentally by microelectrochemical analysis and kinetic studies.

Besides reaction energies the Mulliken charge population analysis was performed to obtain the charge distribution resulting due to the incorporation of N-atoms in the graphitic carbon framework which showed a negative charge of -0.32 e over the N-atom and positive charge of 0.21 e over the carbon atom neighbouring nitrogen (Fig. S5a, SI). This explains the presence of electronic anisotropy in the catalyst due to strong electronegativity of nitrogen atom and hence the resultant activity *versus* the nitrogen-deficient system. The interaction occurring as a result of this nitrogen induced anisotropy is also illustrated in Fig. S5b (SI) in the form of a molecular electrostatic potential (MEP) map wherein the red regions denote electron rich sites (N-species) and the neighbouring carbon atoms exhibit yellow contour depicting positive charge and hence interacts with the incoming O₂ to yield NCS-OOH species eventually facilitating ORR.

Following charge distribution, energy separation between the highest occupied molecular orbital (HOMO) and lowest unoccupied molecular orbital (LUMO) was computed to be 1.68 eV before and 1.04 eV after nitrogen insertion. Smaller HOMO-LUMO gap for the NCS catalyst signifies increased chemical reactivity leading to a facile activated species formation which eventually gets converted to the product effectuating catalysis. Similar results were obtained in terms of stepwise transformation of adsorbed O₂ wherein the reaction energy becomes increasingly negative advancing towards the more stable product via. H₂O₂ species formation. Therefore, even a very small amount of nitrogen insertion (2.66%) into the graphitic framework of carbon induced charge redistribution for active site generation facilitating a 2+2 reduction pathway for oxygen.

➤ **Sample-generation tip-collection (SG-TC) analysis:**

A 4-probe microelectrochemical assay was performed over the NCS-800 coated GC plate (NCS-800/GC-plate; WE1) being investigated by Pt microelectrode tip (\varnothing 10 μm ; WE2) using a Pt coil counter electrode and referenced against Ag/AgCl/3M KCl electrode (potentials are converted to RHE scale). The resultant 4 electrode set-up with two working electrodes dipped in 1 M NaOH electrolyte was analysed towards its ORR activity in a generator-collector mode. The NCS-800/GC-plate acted as the sample (WE1, generator) whose local ORR activity was analysed using the Pt ultramicroelectrode (WE2, tip) which served as a collector that determines the intermediate involved during the ORR process. The Pt-tip was precisely positioned vertically in very close proximity (10 μm) above the NCS-800 catalyst spot to ensure the collection of any peroxide intermediate produced in the gap between WE1 and WE2 during the ORR process. Initially, cyclic voltammetry was performed at WE1 from 1.4 V to 0.1 V (vs. RHE) while concomitantly applied a constant potential of 1.4 V (vs. RHE) at WE2 throughout the CV to collect any H_2O_2 produced during ORR at WE1 that convert back to O_2 (by showing an oxidative current for oxidation of H_2O_2 back to O_2). Fig. 2a depicts this response where the oxygen reduction current is observed at WE1 and a simultaneous upsurge in the oxidation current was observed at WE2 resulting from the generated H_2O_2 which can be used as a marker for delimiting ORR onset potential.

This initial indicative experiment was followed by performing a sequential-pulse chronoamperometric measurement in the same experimental set-up. The WE1 (NCS-800/GC, sample) was polarized at 1.43 V (vs. RHE) for 2 min. and the current response was recorded at WE2 (tip) at a fixed potential of 1.4 V (vs. RHE). Subsequently, the potential at WE1 was stepped down by 50 mV (i.e., from 1.43 to 1.38 V) and again held for 2 min. The measurement was continued with sequential decrease in potential having a potential width of 50 mV interval till 0.13 V (i.e., at every 50 mV the sample was polarized for 2 min and current was recorded at the tip). The Pt-tip was constantly polarized at 1.4 V throughout the experiment to probe any increase in oxidation current indicating H_2O_2 generation and hence ORR onset. Fig. 2b portrays this response wherein the lower portion displays the chronoamperometric current at WE1 (where the reduction of oxygen takes place) and the colored arrows indicate the different reduction potential steps applied at each 2 min. interval. Simultaneous current measured at WE2 (held at 1.43 V) during the sequential change in WE1 potential is represented in the top portion of Fig. 2b where the different colored segments correspond to the potential step indicated by same colored arrow in the lower portion. A rapid upsurge in the ORR current at WE1 starts at 0.985 V (vs. RHE) indicating ORR onset potential which is further supported by a simultaneous increase in oxidative current at WE2 corresponding to H_2O_2 production. This oxidative current at WE2 remains constant up to 0.43 V but thereafter decreases to the base current and further remained same at more negative potentials. The occurrence of oxidative wave followed by its fall suggests that the ORR over NCS-800 follows a 2+2 electron pathway involving an H_2O_2 intermediate.

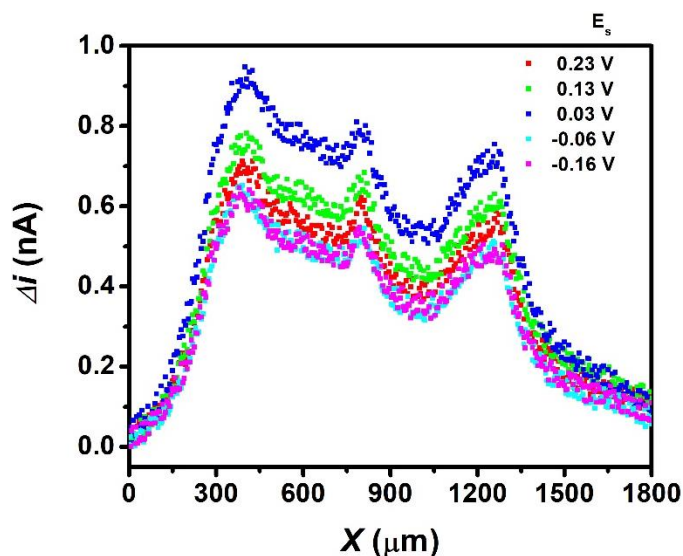


Fig. S6. Baseline-corrected RC-SECM x-line scans (at $y = 600 \mu\text{m}$) of NCS-800 for optimization of sample polarization potential (E_s) ranging from 0.23 V to -0.16 V (at $E_{\text{tip}} = 0.03 \text{ V}$) with a step of $5 \mu\text{m}$ and $10 \mu\text{m/s}$ speed. CE: Pt-coil; RE: Ag/AgCl/3 M KCl (potentials converted to RHE scale).

➤ 2D RC-SECM Imaging:

The localized visualization of electrocatalytic activity of the NCS catalysts *w.r.t.* its distribution over the coated working electrode can be imaged in a 2D plane as an effective activity descriptor using a 4-probe microelectrochemical assay. Analysis by using this technique gives a demarcation of the electrochemically active region within the catalyst spot (region where catalyst is drop-casted *ca.* $600 \mu\text{m}$) and the unmodified electrode surface, since only the catalyst is active for the electrochemical reaction under study. The set-up is composed of two working electrodes, a Pt coil counter electrode and a Ag/AgCl/3M KCl reference electrode (potentials converted to RHE scale) dipped in 0.1 M NaOH. Sample comprising of the glassy carbon (GC) plate coated with NCS catalyst spot act as Working electrode 1 (WE1) while the other is the Pt-ultramicroelectrode probe ($\varnothing 10 \mu\text{m}$) as WE2 which electrochemically scans a specified region of the substrate spanning the catalyst. The probe subsequently performs an x-y raster scan covering the catalyst spot ($1500 \mu\text{m} \times 1500 \mu\text{m}$) at a height of $15 \mu\text{m}$ from the substrate, at every $10 \mu\text{m}$ distance (grid point). During SECM imaging both the sample (WE 1) and tip (WE2) were constantly polarized in their respective diffusion limited ORR potential region, WE1 at 0.03 V (*vs.* RHE; as per Figure S6) and WE2 at 0.53 V (*vs.* RHE). Both the working electrodes tend to compete for the available dissolved O_2 in the $15 \mu\text{m}$ gap between the probe and the underlying sample (as both are polarised in the diffusion limited region). When tip passes over the active

catalyst zones where the electrolyte was depleted of oxygen (because it was electroreduced by the catalyst) lower tip currents (higher reduction current) were recorded, while higher currents were observed over the zones rich in oxygen. The image colors change from red through yellow-green to blue-violet with decreasing the reduction current (Fig. 4b & S7, SI).

At every grid point both the working electrodes perform ORR and their respective reduction current is recorded, however the probe current is used for activity comparison. This electrochemical response when plotted in a coloured 2D format changes from blue-violet through green-yellow to red indicating sequential decrease in reduction current at the probe and hence increased ORR activity of the catalyst. Essentially, the bright red region in the 2D RC-SECM trace indicates competitively active catalyst-coated region against the unmodified GC plate region exhibiting blue colour. This localized analysis also reveals the distribution of active sites over the catalyst spot apart from its competitive activity towards ORR. If the electrochemical current response over the catalyst spot is uniform, resulting in an even red spot it indicates that the active sites are homogeneously distributed over the catalyst.

The 2D RC-SECM response for the prepared NCS catalysts are depicted in Fig. 4b (manuscript) & S7 (SI) portraying differential ORR activity. The 2D plot for NCS-600 depicts green colouration with faint red regions indicating poor ORR activity, however the response is improved for NCS-700 but it exhibits uneven active site distribution as shown by localized red spots. The maximal activity is obtained for NCS-800 with a high ORR current and in turn reduced probe current with uniform red colour taking the shape of the catalyst spot vindicating evenly distributed active sites. The response for NCS-900 matches with that observed for NCS-600 showing green colouration and hence poor activity. Therefore, NCS-800 emerges out to be the highly active catalyst amongst the NCS variants with a uniform distribution of active sites displaying a well resolved 2D RC-SECM image.

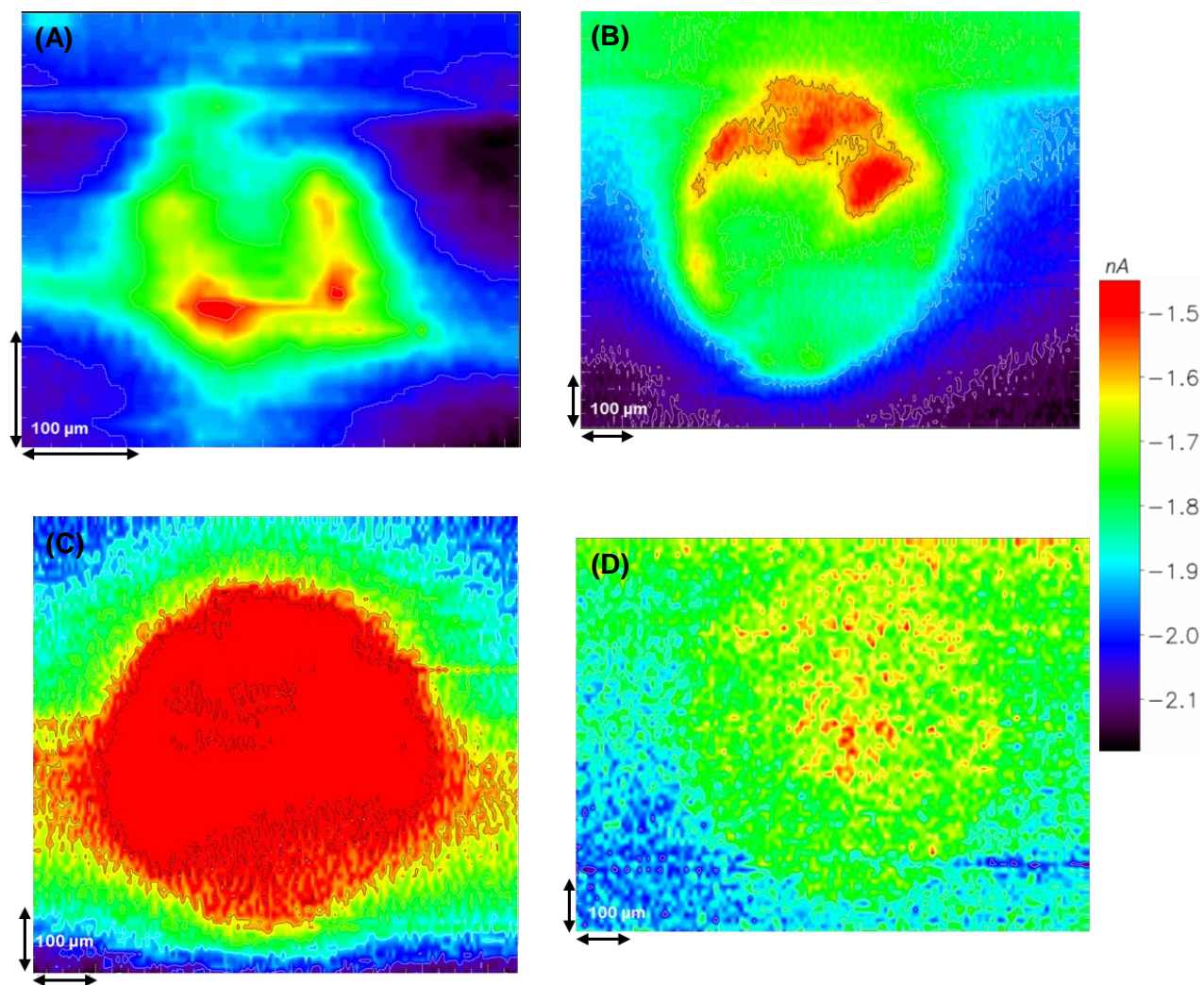


Fig. S7. 2-D RC-SECM for ORR over (a) NCS-600, (b) NCS-700, (c) NCS-800 and (d) NCS-900 where WE1 is polarized at 0.03 V while competing with Pt-tip (WE2 polarized at 0.53 V) for available dissolved oxygen in 0.1 M NaOH electrolyte. CE: Pt coil; RE: Ag/AgCl/3 M KCl (potentials converted to RHE scale).

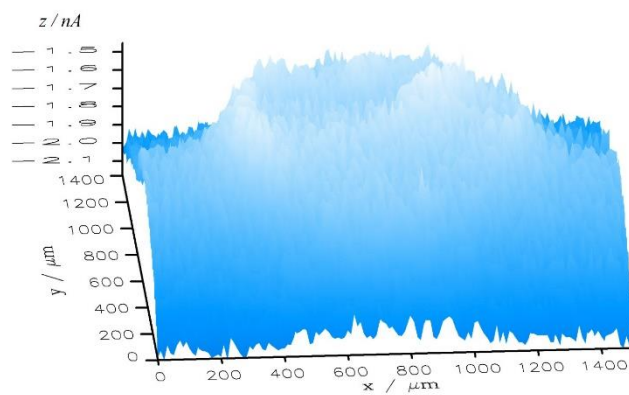


Fig. S8. 3-D projection of RC-SECM image for ORR by NCS-800 in 0.1 M NaOH electrolyte at a potential of 0.03 V on WE1 and 0.53 V on WE2. CE: Pt coil; RE: Ag/AgCl/3M KCl (Potentials are converted to RHE scale).

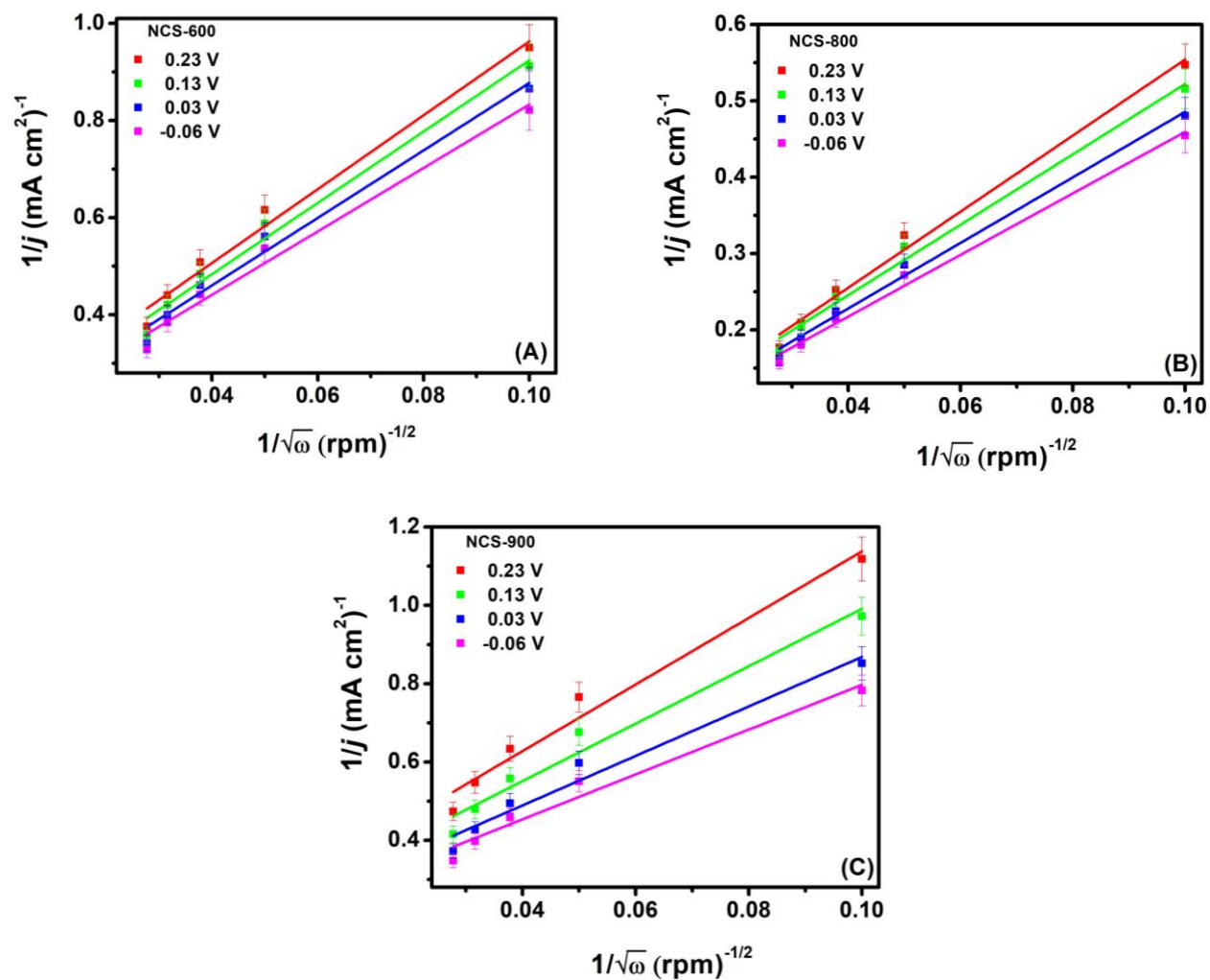


Fig. S9. The Koutecky-Levich plot for (a) NCS-600, (b) NCS-800 and (c) NCS-900 catalysts at varying potentials derived from the linear polarization curves at different rotation rates. (Potentials converted to RHE scale)

➤ **Koutecky-Levich Analysis:**

The linear polarization curves obtained while performing rotating disk electrode (RDE) measurements as shown in Fig. S2 (SI) can be analyzed further to obtain an important kinetic parameter for ORR *viz.* the number of electrons by employing Koutecky-Levich equation³:

$$\frac{1}{j} = \frac{1}{j_d} + \frac{1}{j_k} = \frac{1}{B\sqrt{\omega}} + \frac{1}{j_k} \quad (1)$$

Where, the measured current density is represented as '*j*' whereas '*j_d*' and '*j_k*' are kinetic and diffusion-limited current densities respectively. The term '*ω*' is the angular rotation rate of the electrode being roated and the entity '*B*' can be elaborated as³:

$$B = 0.62 n F A D^{2/3} \gamma^{-1/6} C \quad (2)$$

Where, '*n*' denotes the number of electrons, '*F*' is the Faraday constant (96500 C/mol), '*A*' is the area of the electrode (here, 0.0707 cm²), '*D*' is the oxygen diffusion coefficient (1.43 x 10⁻⁵ cm²/s), '*γ*' is the kinematic viscosity of the electrolyte (1.13 x10⁻² cm²/s) and '*C*' is the bulk concentration of oxygen in the electrolyte medium (0.843 x10⁻⁶ mol/cm⁻³).

A plot between 1/*j* vs. 1/√*ω* as given in Fig. S9 (SI) and Fig. 5a (manuscript) is a straight line whose slope gives the value of '1/*B*' which can further be used to compute the number of electrons transferred during the potential dependent ORR detailed in Table S1. Consequently, the number of electrons involved for the case of NCS-800 approaches 4 right from the start of the diffusion limited region whereas for the other two it remained nearly a 2 e⁻ process. This suggests an overall conversion of oxygen to water *via.* a 4 e⁻ pathway over NCS-800.

| Table S1: Koutecky-Levich Analysis. | | | |
|--|------------------------------------|----------------|----------------|
| Potential Applied (V vs. RHE) | No. of electrons (<i>n</i>) | | |
| | NCS-600 | NCS-800 | NCS-900 |
| 0.23 | 2.09 | 3.18 | 1.86 |
| 0.13 | 2.17 | 3.40 | 2.16 |
| 0.03 | 2.28 | 3.69 | 2.50 |
| -0.06 | 2.42 | 3.93 | 2.76 |

➤ **Rotating ring-disk Analysis:**

RRDE voltammograms were obtained by performing oxygen reduction linear sweep voltammetry at the disk electrode while polarizing the ring around it at a constant potential of 1.4 V (vs. RHE) to oxidize back any formed H₂O₂ reaching out to the ring from disk electrode (Fig. S4, SI and Fig. 1c, manuscript). The collection efficiency (*N*) of the ring was determined by performing RRDE measurement in a [Fe(CN)₆]^{4-/3-} redox medium and was found to be 0.38.⁴ This '*N*' was subsequently employed to determine the number of electrons transferred '*n*' and % H₂O₂ produced during the oxygen reduction process as follows³:

$$n = 4 I_d / [I_d + (I_r/N)] \quad (3)$$

$$\% \text{H}_2\text{O}_2 = 200 \times (I_r/N) / [I_d + (I_r/N)] \quad (4)$$

Where, '*I_d*' and '*I_r*' denote the disk and the ring currents respectively. These results are collectively presented in Table S2 for all the three catalysts analyzed.

| Table S2: RRDE Analysis. | | | | | | |
|--|----------------|---------------------------------|----------------|---------------------------------|----------------|---------------------------------|
| Potential Applied (V vs. RHE) | NCS-600 | | NCS-800 | | NCS-900 | |
| | <i>n</i> | % H ₂ O ₂ | <i>n</i> | % H ₂ O ₂ | <i>n</i> | % H ₂ O ₂ |
| 0.23 | 2.59 | 70.7 | 3.46 | 27.0 | 2.36 | 81.8 |
| 0.13 | 2.50 | 75.2 | 3.50 | 25.2 | 2.42 | 78.8 |
| 0.03 | 2.62 | 69.0 | 3.60 | 15.8 | 2.46 | 77.1 |
| -0.06 | 2.62 | 69.0 | 3.81 | 11.7 | 2.54 | 73.0 |

➤ **Kinetic Analysis:**

Kinetics of oxygen reduction over NCS-800 was further extended to determine the reaction facility and its rate. These physical entities aid in analyzing the reaction closely and is a marker for its electrochemical activity. Initially, Tafel analysis was performed for the cathodic reaction as per the following equation:⁵

$$\ln j = \ln j_0 - (\alpha n f) \eta \quad (5)$$

$$f = F/RT \quad (6)$$

Where, ' j ' is the kinetic current density, ' j_0 ' is the exchange current density, ' α ' is the electron transfer coefficient, ' n ' is the number of electrons transferred, ' η ' is the overpotential for ORR *w.r.t* the Nernstian potential, ' F ' is the Faraday constant, ' R ' is the gas constant and ' T ' is the temperature. A plot of $\ln j$ vs. η gives the Tafel plot (Fig. 5b, manuscript), whose slope is a major kinetic indicator as it gives a Tafel slope of 62.5 mV/dec in the lower overpotential region and 120.5 mV/dec in the high overpotential region, which are quite close to the ideal values for optimal ORR kinetics. Besides, Tafel slope the intercept of obtained Tafel plot gave the exchange current density ' j_0 ' which for NCS-800 was 6.74×10^{-6} A/cm² and signifying a faster pace of ORR electron transfer kinetics. The Tafel slope can also be used to attain the transfer coefficient as:

$$\alpha = -\left(\frac{\text{Slope}}{nf}\right) \quad (7)$$

This charge transfer coefficient (α) for the rate limiting step of 1 e- transfer to the adsorbed O₂ was determined to be 0.41 at the reaction equilibrium indicating a high probability of the forward reaction to yield product.

Another important aspect was the determination of rate constant ' k ' towards reduction of oxygen as follows:⁵

$$I_k = nFAkC_\infty \quad (8)$$

$$k = I_k/nFAC_\infty \quad (9)$$

Where,

$$I_k = \frac{I_{lim.} \times I}{I_{lim.} - I} \quad (10)$$

Here, ' I_k ' is the kinetic current, ' n ' is the number of electrons transferred in the rate determining step, ' F ' is the Faraday constant, ' A ' is the area of the electrode, ' k ' is the rate constant, ' C_∞ ' is the concentration of oxygen in the bulk of electrolyte, ' I ' is the measured current and ' $I_{lim.}$ ' is the diffusion limited current.

Standard electrochemical rate constant (k_0) was computed using the following equation:

$$k = k_0 \exp(-\alpha n f \eta) \quad (11)$$

$$k_0 = k/\exp(-\alpha n f \eta) \quad (12)$$

Where all the constants have their usual meaning as described above. The value of ' k_0 ' is a measure of catalyst kinetics as to how fast it establishes equilibrium at low overpotentials, higher the value faster is the catalyst towards performing oxygen electroreduction.

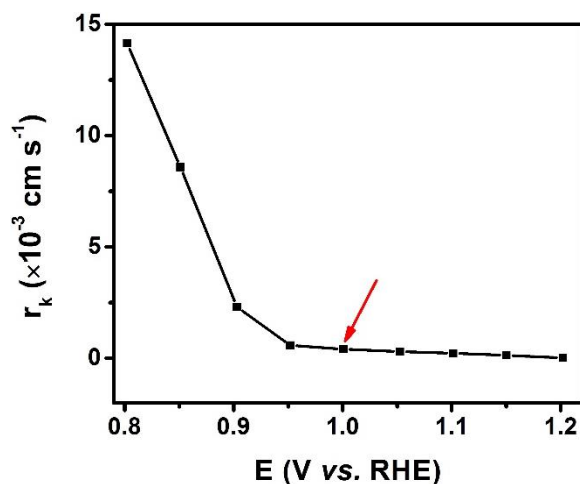


Fig. S10. Potential-dependent ORR rate constant (k) for NCS-800 (arrow marks ORR onset) derived from RDE measurements (Fig. 1b).

➤ **Electrochemical impedance spectroscopy (EIS) analysis:**

EIS study was performed for NCS-600, NCS-800 and NCS-900 in the frequency range from 0.1 Hz to 100 kHz in a 5 mM $\text{K}_4[\text{Fe}(\text{CN})_6] \cdot 3\text{H}_2\text{O}$ solution prepared in 1 M NaOH at its formal potential to obtain the resistances operating in the solution and at the interface (Fig. S11). The analysis yielded a Nyquist plot with a small semicircle and a stout tail in the low frequency range. Solution resistance (R_s) was the high frequency intercept of the real axis, whereas the intercept at low frequency gave polarization resistance (R_p) and the difference between these two gave the charge transfer resistance (R_{ct}), as the hindrance towards electron transfer processes. Thus, lower the value of these resistances better is the charge transfer process and so is the catalyst kinetics.

The fitting of the obtained Nyquist plot was done in to a $[R(Q[RW])]$ circuit and the results are represented in Fig. S11 and Table S3.

| Table S3: EIS Analysis. | | | | |
|--------------------------------|---|---|--|----------------------------|
| Catalyst | R_s (Ω) | R_p (Ω) | R_{ct} (Ω) | χ^2 |
| NCS-600 | 8.1 | 219.3 | 211.2 | 0.1 |
| NCS-800 | 8.1 | 141.2 | 133.1 | 0.1 |
| NCS-900 | 9.8 | 379.0 | 369.2 | 0.1 |

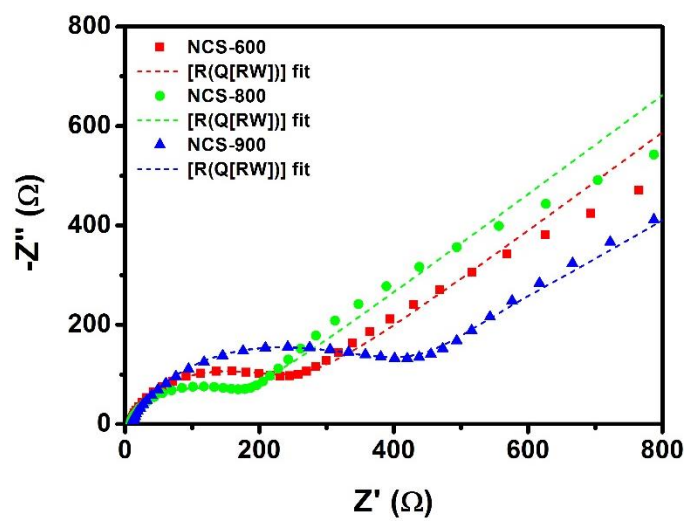


Fig. S11. Fitted Nyquist plot for NCS-600, NCS-800 and NCS-900 catalysts in 5 mM $K_4[Fe(CN)_6] \cdot 3H_2O$ prepared in 1 M NaOH.

➤ **Electrochemical surface area analysis:**

The ECSA available to actively participate in ORR was determined by performing a series of cyclic voltammograms at different scan rates in a non-faradic potential window for all the three-catalyst species *viz.* NCS-600, NCS-800 and NCS-900 respectively (Fig. S12, SI). The experiment was performed in 1 M NaOH and the double-layer pseudo-capacitance (C_{dl}) was determined from the slope of a derived plot between average current density $[(I_a+I_c)/2]$; 'a' denotes anodic current and 'c' is for cathodic current] at 0 V (vs. Hg/HgO) vs. the scan rate, which was linear and the slope yielded C_{dl} which when divided by the specific capacitance of planar surface (40×10^{-6} F/cm²) provided the ECSA.⁶ This ECSA when normalized with the catalyst loading resulted in the specific surface area which is an effective activity descriptor of the catalyst and is comparable with other reported materials.⁷⁻⁹ Another measure of the surface area is roughness factor (R_f) which is obtained upon dividing the ECSA by the geometric area of the working electrode (0.0707 cm²).

| Catalyst | ECSA (cm²) | Specific surface area (m²/g) | R_f (a.u.) |
|-----------------|------------------------------|--|-----------------------------|
| NCS-600 | 1.66 | 3.32 | 23.5 |
| NCS-800 | 7.61 | 15.22 | 107.6 |
| NCS-900 | 0.55 | 1.1 | 7.8 |

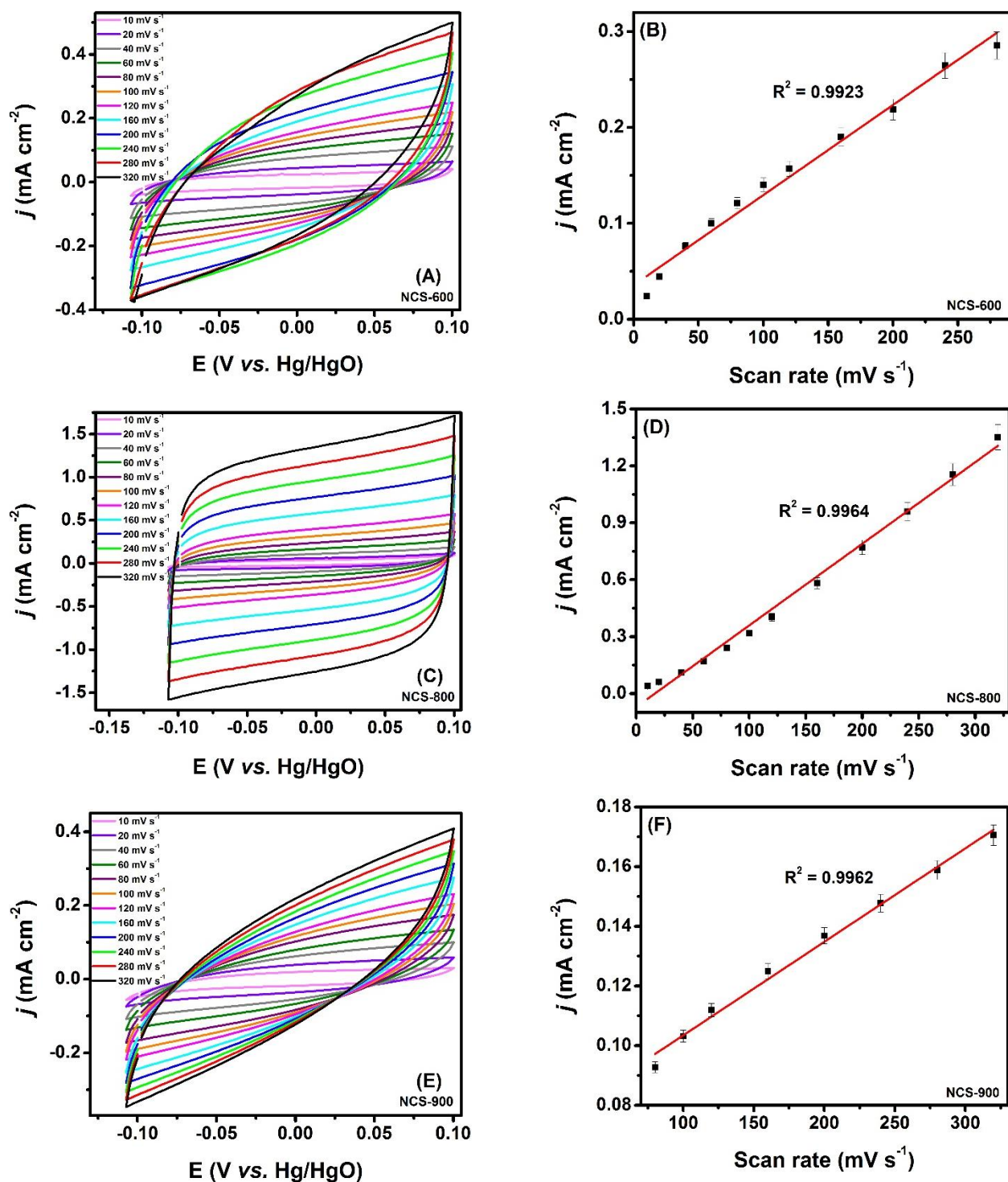


Fig. S12. Cyclic voltammogram in the non-faradic potential region at varying scan rates and the corresponding plot of average current density vs. scan rate for (a, b) NCS-600; (c, d) NCS-800 and (e, f) NCS-900 respectively in 1 M NaOH. CE: Pt-mesh; RE: Hg/HgO/1 M NaOH.

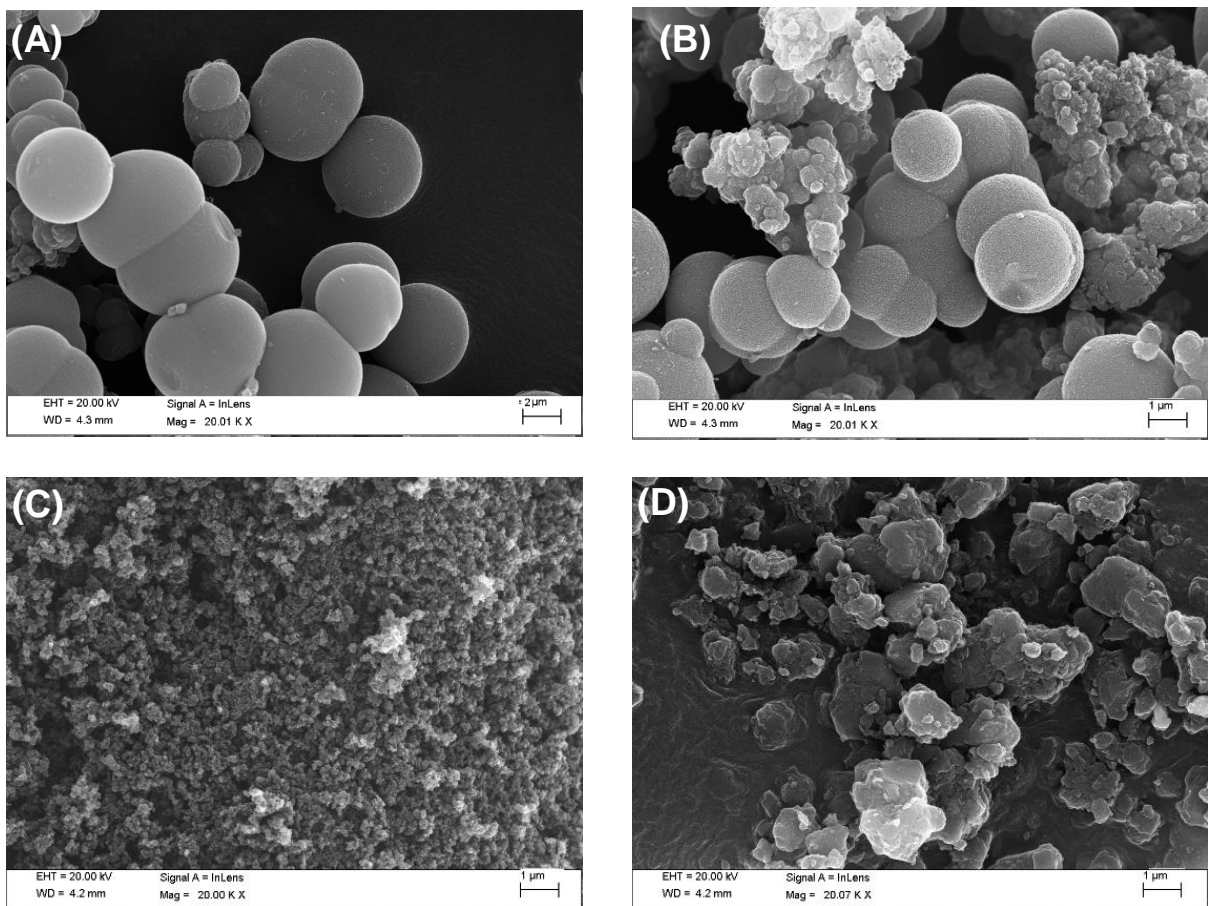


Fig. S13. FE-SEM images of (a) NCS precursor, (b) NCS-600, (c) NCS-800 and (d) NCS-900 respectively.

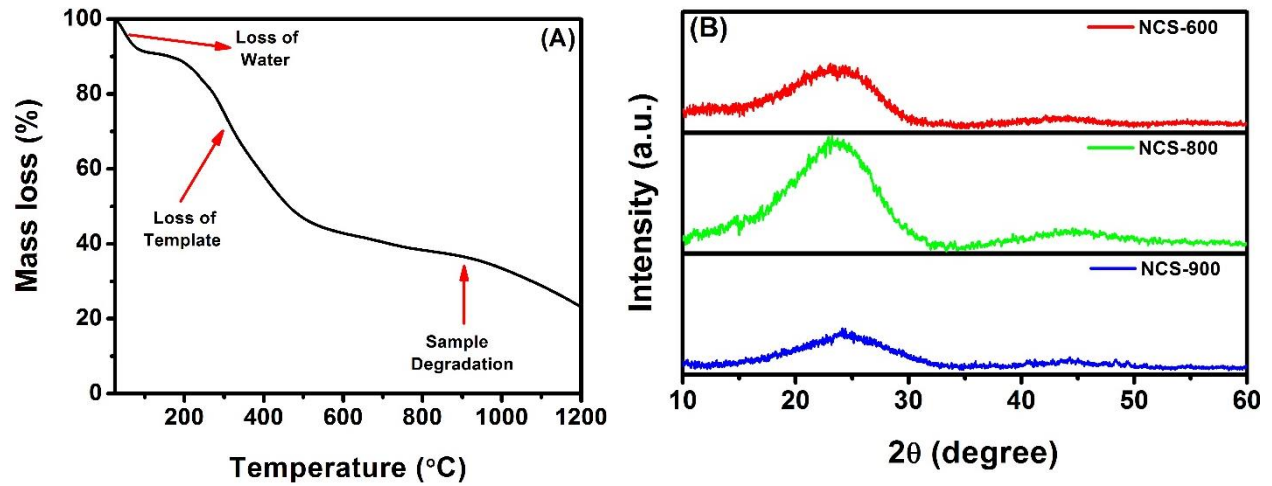


Fig. S14. (a) Thermogravimetric analysis (TGA) of untreated NCS precursor and (b) XRD pattern obtained for NCS-600, NCS-800 and NCS-900 respectively.

| Table S5: Elemental analysis. | | | | |
|-------------------------------|---|---------|---------|---------|
| CoPOM-PVIM Analysis | | NCS-600 | NCS-800 | NCS-900 |
| XPS | C | 90.94 | 97.34 | - |
| | N | 9.06 | 2.66 | - |
| EDAX | C | 90.70 | 96.93 | 97.75 |
| | N | 9.30 | 3.07 | 2.25 |
| CHN | C | 89.95 | 97.10 | 97.95 |
| | N | 10.05 | 2.90 | 2.05 |

| Table S6: XPS deconvolution analysis. | | | |
|--|--|-----------|--------------------------|
| Catalyst | Group | B.E. (eV) | Surface atomic conc. (%) |
| NCS-800 (N: 2.66 %) (C: 97.34 %) | Pyridinic-N | 398.4 | 34.77 |
| | Pyrrolic-N | 399.4 | 18.71 |
| | Graphitic-N | 401.0 | 46.52 |
| | C-C sp ² | 284.6 | 73.85 |
| | C-N sp ² /C-C sp ³ | 285.8 | 26.15 |
| NCS-600 (N: 9.06 %) (C: 90.94 %) | Pyridinic-N | 398.1 | 33.81 |
| | Pyrrolic-N | 399.8 | 30.91 |
| | Graphitic-N | 400.5 | 35.28 |
| | C-C sp ² | 284.3 | 44.78 |
| | C-N sp ² /C-C sp ³ | 285.1 | 55.22 |

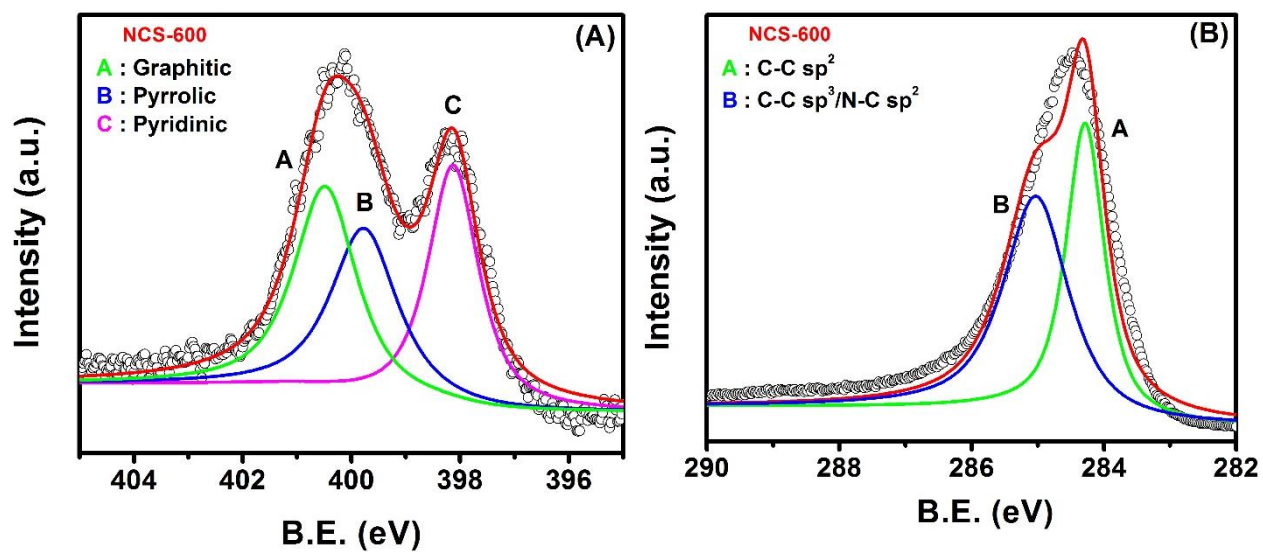


Fig. S15. Deconvoluted XPS spectra of (a) N1s and (b) C1s present in NCS-600 respectively.

| Table S7: ORR performance of various electrocatalyst in alkaline medium. | | | |
|---|---|--------------------------------------|---------------------|
| Catalyst | Synthetic approach | E_{onset} (V vs. RHE) | Ref. |
| Platinum-group metals | | | |
| Pt/C (20 wt%) | E-TEK | 1.07 | 10 |
| Pt/VC | Commercial | 0.93 | 11 |
| Pt-Pd | Sol-gel | 0.97 | 12 |
| Au@Pd/rGO | One-step wet chemical method | 0.90 | 13 |
| Pd/C | Pyrolysis at different temperature (300-600°C) | 0.97 | 14 |
| Transition-metal doped carbon | | | |
| Fe-N/C | Pyrolysis at 800, 900 and 950° C under N ₂ and NH ₃ followed by treatment with HF | 0.90 | 15 |
| Co ₃ O ₄ /N/C | Pyrolysis of Co-MOF for 12h at 800°C | 0.92 | 16 |
| Co-N/C | Pyrolysis of Vitamin B12 at 900° C in N ₂ environment | 0.91 | 17 |
| Mn ₃ O ₄ /N/C | Multistep process, involving calcination, hydrothermal and pyrolysis at 1000 °C | 0.91 | 18 |
| Fe-Carbon nitride "Core shell" | FeCl ₃ and K ₄ {Fe(CN) ₆ } as Fe source with Sucrose as carbon followed by pyrolysis at different temperatures | 0.90 | 19 |
| Nitrogen-doped carbon | | | |
| 3-D Nitrogen-doped graphene | Pyrolysis of GO with Ppy at different temperatures (800-1000 °C) | 0.84 | 20 |
| Nitrogen-doped carbon fiber | Multistep process, involving electrospinning, carbonization at 1000 °C followed by acidification and treatment with ammonia | 0.96 | 21 |
| Nitrogen-doped carbon nanosheets | Graphene-silica nanosheets followed by surface coating with polydopamine (PDA) and pyrolysis at different temperature (800-1000 °C) | 0.96 | 22 |
| Nitrogen-doped MWCNT | Ex situ functionalization of MWCNT <i>via</i> . aryldiazonium chemistry | 0.83 | 23 |
| Nitrogen-doped graphene and MWCNT | Multi-step involving functionalization of graphene followed by pyrolysis at 800 °C with MWCNT | 0.91 | 24 |
| NCS-800 | Simple synthetic approach for preparing nitrogen containing carbon spheres without additional post-treatment | 0.985 | Present work |

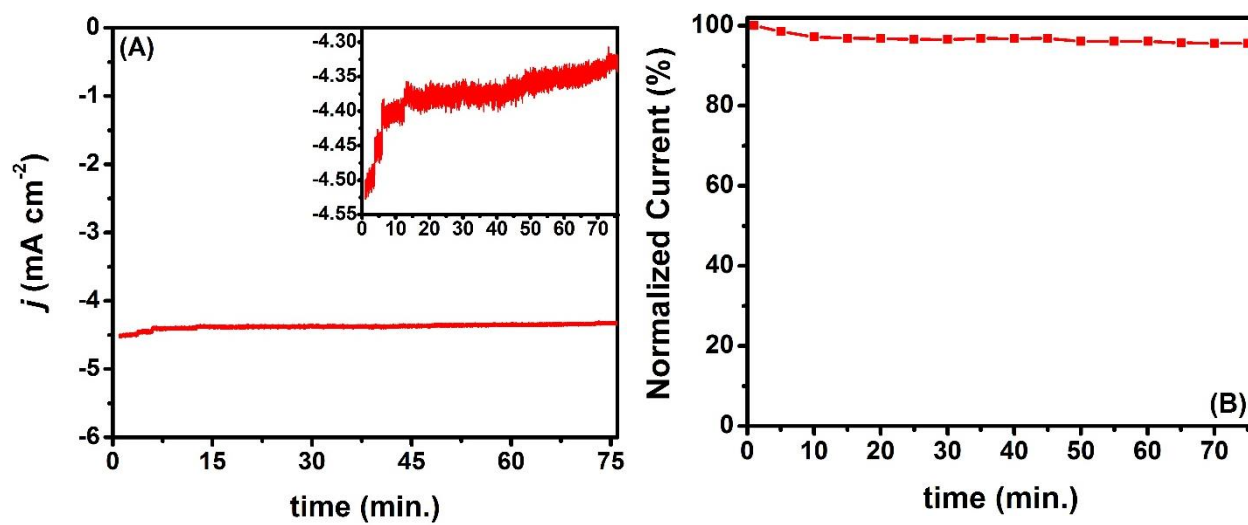


Fig. S16. (a) Chronoamperometric stability analysis of NCS-800 towards ORR in oxygen saturated 1 M methanol solution prepared in 1 M NaOH at 0.43 V for 75 minutes, and (b) normalized current *versus* time response. CE: Pt mesh; RE: Hg/HgO/1M NaOH (potential converted to RHE scale).

References:

- 1 W. R. Wadt and P. J. Hay, *J. Chem. Phys.*, 1985, **82**, 284-298.
- 2 P. J. Hay and W. R. Wadt, *J. Chem. Phys.*, 1985, **82**, 270-283.
- 3 A. Tiwari and T. C. Nagaiah, *ChemCatChem*, 2016, **8**, 396-403.
- 4 A. Tiwari, T. C. Nagaiah and A. Bordoloi, *ChemPlusChem*, 2015, **80**, 1666-1672.
- 5 A. J. Bard and L. R. Faulkner, *Electrochemical Methods: Fundamentals and Applications*, Wiley, 2000.
- 6 J. Kibsgaard, C. Tsai, K. Chan, J. D. Benck, J. K. Nørskov, F. Abild-Pedersen and T. F. Jaramillo, *Energy Environ. Sci.*, 2015, **8**, 3022-3029.
- 7 M. Oezaslan, F. Hasché and P. Strasser, *J. Electrochem. Soc.*, 2012, **159**, B394-B405.
- 8 X. Xu, C. Tan, H. Liu, F. Wang, Z. Li, J. Liu and J. Ji, *J. Electroanal. Chem.*, 2013, **696**, 9-14.
- 9 E. Negro, K. Vezzù, F. Bertasi, P. Schiavuta, L. Toniolo, S. Polizzi and V. Di Noto, *ChemElectroChem*, 2014, **1**, 1359-1369.
- 10 J. Perez, E. R. Gonzalez and E. A. Ticianelli, *Electrochim. Acta*, 1998, **44**, 1329-1339.
- 11 R. Jäger, E. Härk, P. E. Kasatkin and E. Lust, *J. Electrochem. Soc.*, 2014, **161**, F861-F867.
- 12 C.-L. Lee, C.-C. Yang, C.-R. Liu, Z.-T. Liu and J.-S. Ye, *J. Power Sources*, 2014, **268**, 712-717.
- 13 S.-S. Li, A.-J. Wang, Y.-Y. Hu, K.-M. Fang, J.-R. Chen and J.-J. Feng, *J. Mater. Chem. A*, 2014, **2**, 18177-18183.
- 14 L. Jiang, A. Hsu, D. Chu and R. Chen, *J. Electrochem. Soc.*, 2009, **156**, B643-B649.
- 15 A. Serov, K. Artyushkova, N. I. Andersen, S. Stariha and P. Atanassov, *Electrochim. Acta*, 2015, **179**, 154-160.
- 16 G. Zhang, C. Li, J. Liu, L. Zhou, R. Liu, X. Han, H. Huang, H. Hu, Y. Liu and Z. Kang, *J. Mater. Chem. A*, 2014, **2**, 8184-8189.
- 17 Y. Yang, J. Liu, Y. Han, H. Huang, N. Liu, Y. Liu and Z. Kang, *Phys. Chem. Chem. Phys.*, 2014, **16**, 25350-25357.
- 18 S. Gao and K. Geng, *Nano Energy*, 2014, **6**, 44-50.
- 19 K. Vezzù, A. Bach Delpéuch, E. Negro, S. Polizzi, G. Nawn, F. Bertasi, G. Pagot, K. Artyushkova, P. Atanassov and V. Di Noto, *Electrochim. Acta*, 2016, **222**, 1778-1791.
- 20 Z. Lin, G. H. Waller, Y. Liu, M. Liu and C.-p. Wong, *Nano Energy*, 2013, **2**, 241-248.
- 21 J. Yin, Y. Qiu, J. Yu, X. Zhou and W. Wu, *RSC Adv.*, 2013, **3**, 15655-15663.
- 22 W. Wei, H. Liang, K. Parvez, X. Zhuang, X. Feng and K. Müllen, *Angew. Chem.*, 2014, **126**, 1596-1600.
- 23 G. Tuci, C. Zafferoni, A. Rossin, A. Milella, L. Luconi, M. Innocenti, L. Truong Phuoc, C. Duong-Viet, C. Pham-Huu and G. Giambastiani, *Chem. Mater.*, 2014, **26**, 3460-3470.
- 24 S. Ratso, I. Kruusenberg, M. Vikkisk, U. Joost, E. Shulga, I. Kink, T. Kallio and K. Tammeveski, *Carbon*, 2014, **73**, 361-370.